



Publication Year	2019
Acceptance in OA@INAF	2021-01-27T14:56:10Z
Title	Independent confirmation of a methane spike on Mars and a source region east of Gale Crater
Authors	GIURANNA, MARCO; Viscardy, Sébastien; Daerden, Frank; Neary, Lori; Etiope, Giuseppe; et al.
DOI	10.1038/s41561-019-0331-9
Handle	http://hdl.handle.net/20.500.12386/30044
Journal	NATURE GEOSCIENCE
Number	12

Supplementary Information for:

Independent confirmation of a methane spike on Mars and a source region east of Gale Crater

Marco Giuranna^{1*}, Sébastien Viscardy², Frank Daerden², Lori Neary², Giuseppe Etiope^{3,1}, Dorothy Oehler⁴, Vittorio Formisano[†], Alessandro Aronica¹, Paulina Wolkenberg^{1,5}, Shohei Aoki^{1,2,6,7}, Alejandro Cardesín-Moinelo⁸, Julia Marín-Yaseli de la Parra⁸, Donald Merritt⁸

¹Istituto di Astrofisica e Planetologia Spaziali (INAF-IAPS), Via del Fosso del Cavaliere 100, 00133 Rome, Italy.

²Royal Belgian Institute for Space Aeronomy, Avenue Circulaire 3, 1180 Brussels, Belgium

³Istituto Nazionale di Geofisica e Vulcanologia, via V. Murata 605, 00143 Rome, Italy, and Faculty of Environmental Science and Engineering, Babes-Bolyai University, Cluj-Napoca, Romania

⁴Planetary Science Institute, 1700 East Fort Lowell Road, Tucson, Arizona 85719 USA

⁵Centrum Badan Kosmicznych Polska Akademia Nauk, ul. Bartycka 18a, Warsaw, Poland

⁶Fonds National de la Recherche Scientifique, rue d'Egmont 5, B-1000 Brussels, Belgium

⁷Department of Geophysics, Tohoku University, Sendai, Miyagi 980-8578, Japan.

⁸European Space Astronomy Centre, Villanueva de la Cañada, E-28692, Madrid, Spain

*Corresponding author: marco.giuranna@iaps.inaf.it

SI-1. PFS data selection and treatment

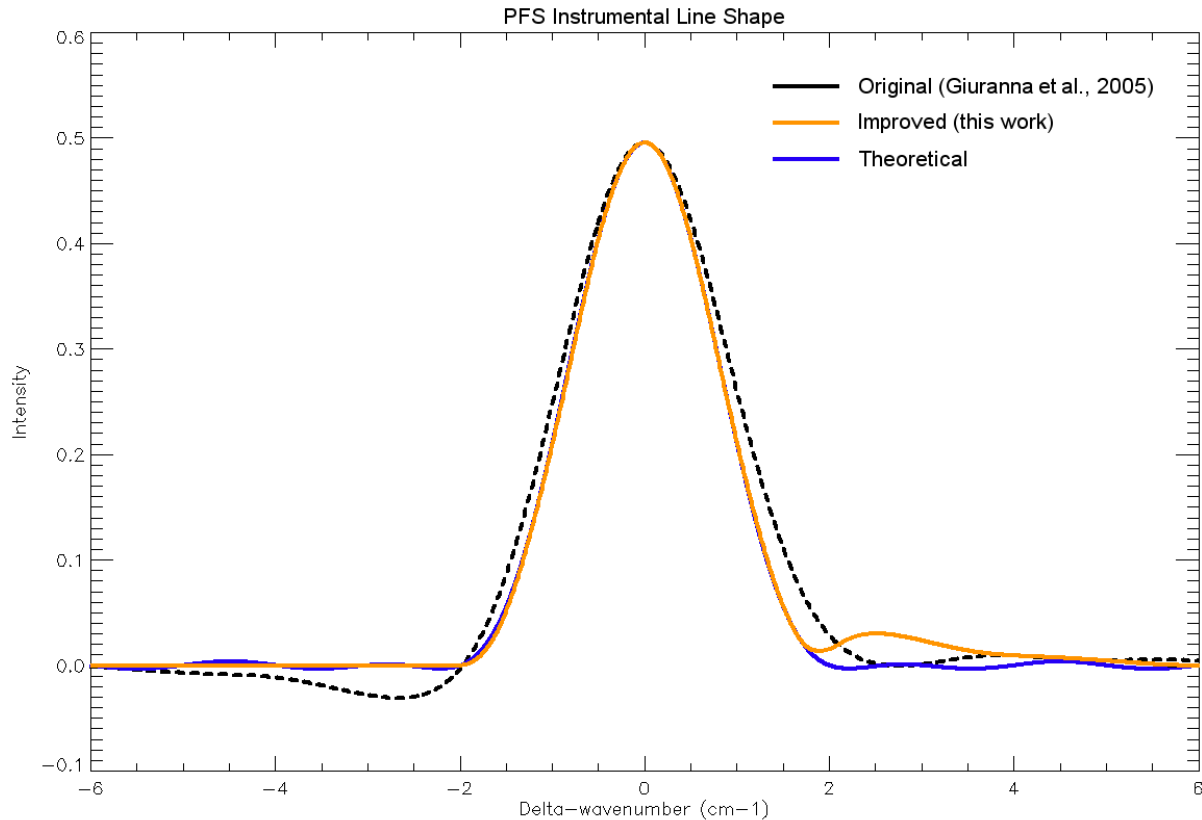
The Planetary Fourier Spectrometer³⁸ (PFS) on Mars Express³⁷ (MEx) is a double-pendulum infrared Fourier spectrometer optimized for atmospheric studies. It has two distinct spectral channels operating simultaneously and covering the wavenumber range between 200–2000 cm^{-1} (Long Wavelength Channel, hereafter LWC) and 2000–8300 cm^{-1} (Short Wavelength Channel, hereafter SWC). Both channels have a sampling step of 1 cm^{-1} and a spectral resolution of $\sim 1.3 \text{ cm}^{-1}$, when no apodization function is applied, and $\sim 1.8 \text{ cm}^{-1}$ when a Hamming function is applied to the measured interferograms (as in the case of the present work). The MEx spacecraft is orbiting Mars in a polar orbit having an inclination of 87° , a pericenter altitude of $\sim 240 \text{ km}$ and an orbital period of 7.5 h. The instantaneous field of view (IFOV) is about 1.52° (full-width half-maximum, FWHM) for the SWC, and 2.69° (FWHM) for the LWC, which corresponds to a spatial resolution of 6.5 and 11.5 km, respectively, at the pericenter. PFS has been observing the martian atmosphere since January of 2004, $L_s = 331.18^\circ$ of MY 26. It has now provided nearly continuous monitoring of conditions in the martian atmosphere for over seven full martian years and it is still performing measurements at the time of writing.

In PFS SWC spectra, methane is detected by identification of the Q-branch² at 3018 cm^{-1} . Due to its weak absorption, relatively low abundance, and high spatial and temporal variability, quantitative analyses of CH_4 with PFS require special attention to the way the spectra are collected, handled, and analyzed. We developed a new approach to PFS data selection, treatment, and retrieval which largely reduces statistical uncertainties of PFS measurements and improves accuracy of CH_4 retrievals. In order to increase the signal-to-noise ratio (SNR) and reduce statistical uncertainties of PFS measurements to be used for quantitative retrievals of CH_4 abundance, we adopted the following procedure:

Step 1: *Hamming apodization function is applied to PFS interferograms.* It is common practice in Fourier transform spectroscopy to multiply the measured interferogram by an apodizing function in order to reduce the amount of ringing present in the resulting instrumental line shape⁷⁷. This reduces the spectral resolution a bit (from 1.3 cm^{-1} to 1.8 cm^{-1} in the case of PFS⁷⁸), but also reduces the instrumental noise and the magnitude of the side-lobes in the instrumental line shape, which are a direct result of the finite maximum optical difference in the measured interferograms⁷⁹. The Hamming function H is defined as $H(\delta/L) = 0.54 + 0.46\cos(\pi\delta/L)$, where δ is the optical path difference out to a maximum value of L .

Step 2: *New retrieval of PFS apodized instrument line shape (ILS).* The ILS of a spectrometer is a very important function that must be well characterized because it can introduce spurious features in the measurements. The PFS ILS was first characterized in the laboratory by looking at a monochromatic source (a mercury lamp⁷⁸). The final result was a function of sinc type, with a FWHM of 1.3 cm^{-1} and strong asymmetric side lobes when no apodization function is applied⁷⁸ (**Fig. S3**), and a quasi-symmetric function with a FWHM of $\sim 2 \text{ cm}^{-1}$ when the Hamming function is applied to the measured interferograms⁷⁸ (**Fig. S1**). We improved the characterization of the PFS apodized instrument line shape originally derived in the laboratory adopting an iterative optimization process⁸⁰. First, an input radiance must be provided. It represents the distorted spectrum measured by the instrument. Contrary to the laboratory, an input radiance with narrow absorption or emission lines is not available on Mars. We then used a set of large PFS average spectra (> 1000 measurements for each average) collected under similar atmospheric conditions (an example is described below and presented in **Fig. S2a**). A synthetic spectrum is then calculated at high resolution (line-by-line calculation, see “Methods” in the main text), so that absorption lines are resolved to their natural shape and best-fitted to the measured input radiance. Once these two sets of data are obtained, the characterization becomes an iterative optimization process on the ILS characterization. As an initial guess for the ILS, we used the apodized instrumental line shape of PFS originally measured in the laboratory⁷⁸ (**Fig. S1**). Once the synthetic distorted spectrum is close to the measured one up to a certain threshold value (i.e., the PFS SWC Noise Equivalent Signal

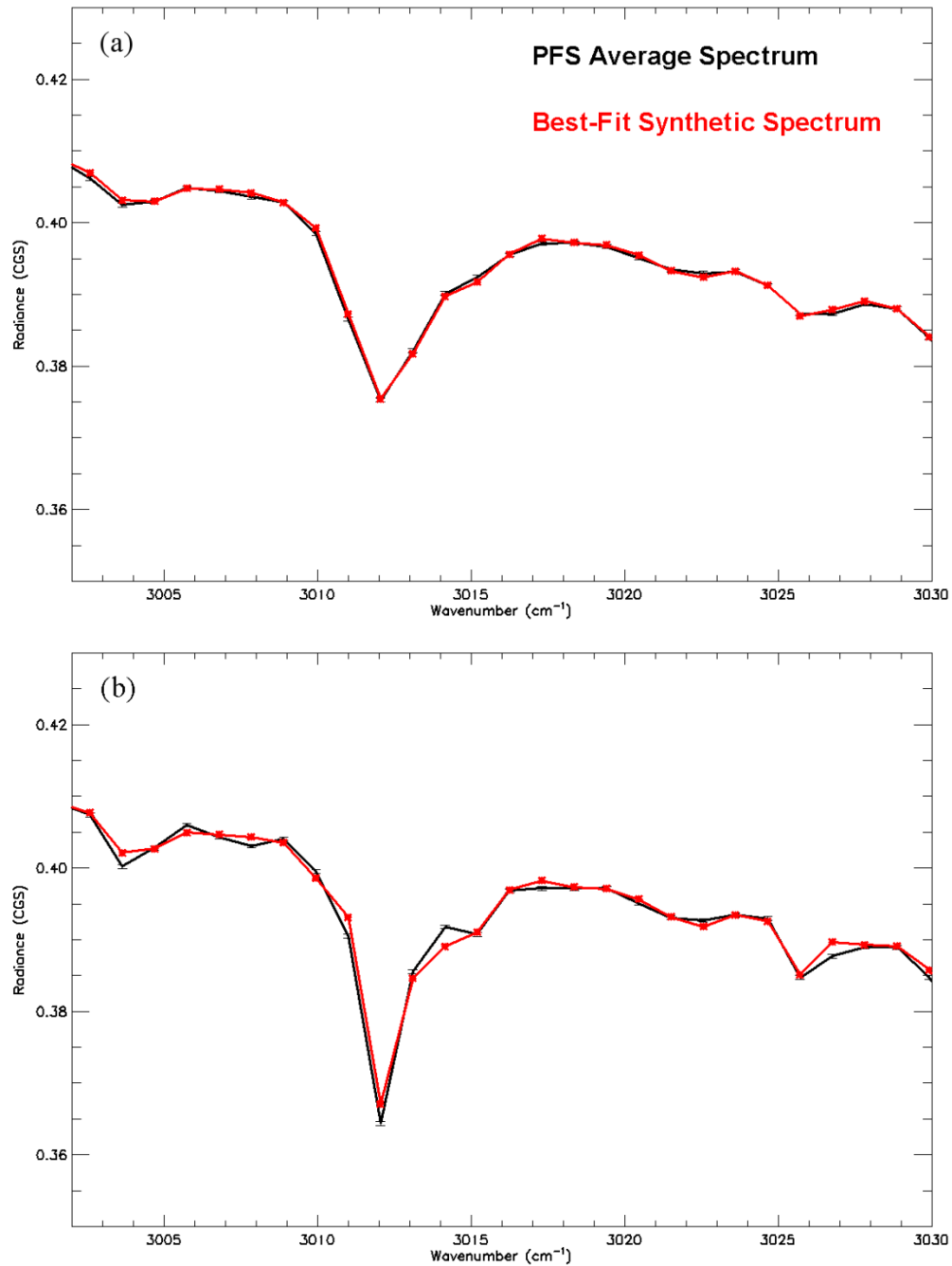
Radiance, NESR, measured on space⁷⁸), the algorithm stops, and the ILS is retrieved. The improved PFS apodized ILS is shown in **Fig. S1** and compared to the original ILS derived in the laboratory. The final result is again a function of sinc type, but with a FWHM of 1.8 cm^{-1} . Interestingly, the improved ILS is similar to the expected theoretical apodized ILS for PFS, except slightly asymmetric (**Fig. S1**).



Supplementary Figure S1: PFS apodized instrumental line shape (ILS). The improved PFS apodized ILS (orange) is compared to the original ILS measured in the laboratory (black dashed) and with the expected theoretical apodized sinc function for PFS (blue).

A representative example of PFS average spectrum used for the characterization of the improved apodized ILS, as well as of the quality of the agreement between the measured and the synthetic best-fit spectra achieved by adopting the new ILS, is shown in **Fig. S2a**. Here we compare a PFS average spectrum to the best-fit synthetic spectrum calculated by means of the radiative transfer code and the retrieval scheme described in the “Methods” section of the main text. The spectrum shown in **Fig. S2a** is an average of 1,350 measurements collected in the various martian years observed by PFS with the following criteria: (a) $0\text{--}10^\circ$ N latitude range; (b) $280\text{--}300^\circ$ L_s range; (c) 8–10 h LT; (d) dust opacity 0.13–0.17. The above selection criteria were adopted with the aim to increase the number of spectra to be co-added with similar atmospheric conditions. Despite the small error bars in the average spectrum due to the large number of spectra co-added, the differences between the PFS average spectrum and the best-fit synthetic spectrum are always within the uncertainty due to the instrumental noise, which is largely reduced by the ensemble average process as described in Step 3 below. Similar considerations apply to the other PFS average spectra utilized as input distorted spectra in the ILS retrieval scheme described above. We remark here that no CH_4 absorption feature is observed in the PFS average spectra used as input radiance for the ILS retrieval process (e.g., **Fig. S2a**). Indeed, given the large spatial and temporal variability of methane

on Mars, no CH₄ feature is expected in these large averages, since the individual spectra were selected at random and include various areas, seasons, and martian years.

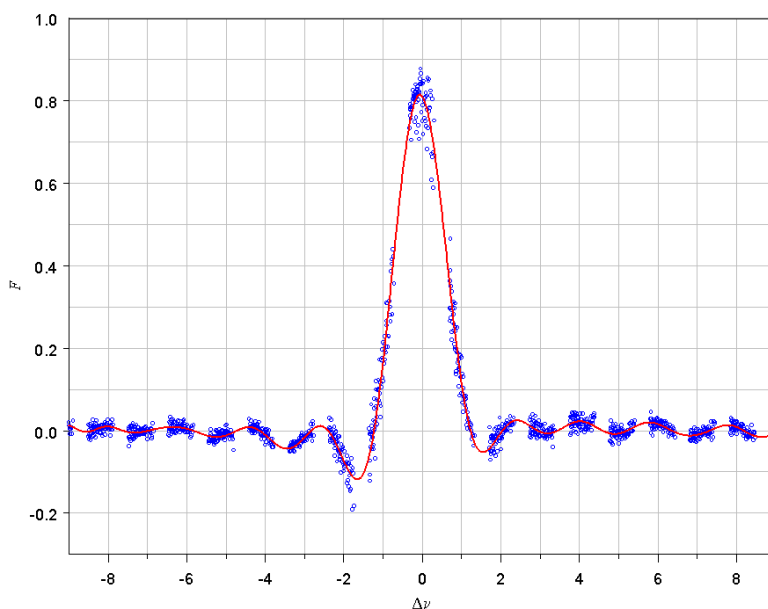


Supplementary Figure S2: Apodized vs unapodized PFS spectra. (a) Comparison of apodized PFS average spectrum (black) to the best-fit synthetic spectrum (red) obtained with the improved apodized ILS. (b) Same as in (a), except for the unapodized PFS spectrum. PFS unapodized ILS originally derived in the laboratory was used for convolution of the high-resolution line-by-line synthetic spectra. See text for more details.

With the adoption of (i) the new PFS data selection and treatment described here (see also Step 3 below), which largely reduces the statistical uncertainties of PFS measurements, the instrumental noise, and the magnitude of the side-lobes in the instrumental line shape, (ii) the improved

characterization of the apodized ILS, and (iii) the advanced retrieval algorithm (see Methods), the agreement between synthetic best-fit and PFS average spectra is typically very good in the entire spectral range considered (e.g., **Figs. 1, S2a, and S12b**).

Previous detections of methane by PFS have been questioned due to some “unidentified” spectral features of similar strength to that of the methane band. We believe it is important to clarify this aspect, and explain that there have never been “unidentified” features in PFS spectra, but rather a poor characterization of the PFS “unapodized” ILS. Indeed, previous analyses made use of unapodized PFS spectra^{2,18,19}. The best-fit synthetic spectra were obtained by convolution of the high-resolution line-by-line spectra and the PFS unapodized ILS derived in the laboratory. As mentioned already, the latter is a function of sinc type with strong and asymmetric side lobes⁷⁸. As a consequence, PFS unapodized spectra contain spurious features due to ringing and/or overshoot⁷⁹. If the unapodized ILS, to which the high-resolution synthetic spectra are convoluted in order to mimic the PFS spectral response and resolution, is well characterized, then this will not be an issue, as the effects of ringing and overshoot will be correctly reproduced in the modelled spectra. On the contrary, if the ILS is not correctly characterized, then the quality of the fit and of the retrieved quantities will be affected. This was the case of the previous analyses. In **Fig. S2b** we show the same spectrum as in **Fig. S2a**, except that no apodization is applied, along with the synthetic best-fit spectrum. The solar and the H₂O lines are more pronounced in the unapodized spectrum due to the increase of the spectral resolution (1.3 cm⁻¹ versus 1.8 cm⁻¹). However, the overall quality of the fit is reduced compared to the apodized case (**Fig. S2a**). Some of the observed spectral features are poorly reproduced by the synthetic spectrum. As anticipated, this is because the PFS unapodized ILS originally retrieved in the laboratory⁷⁸ is not adequately characterized. The latter is shown in **Fig. S3**, where the blue circles represent the measured intensity of the observed monochromatic source (a mercury lamp), and the red line is the fitted curve (unapodized ILS) actually used in the previous analyses.



Supplementary Figure S3: PFS unapodized ILS. PFS unapodized ILS measured in the laboratory with a Hg lamp. Horizontal units are cm⁻¹, vertical is line intensity (from *ref.*⁷⁸).

It appears evident there are not enough measurements to fully characterize the intensity of the main side lobes of the unapodized ILS, and especially for the strong one to the left, which appear to be underestimated in the retrieved ILS (**Fig. 3**). The inaccurate characterization of the PFS

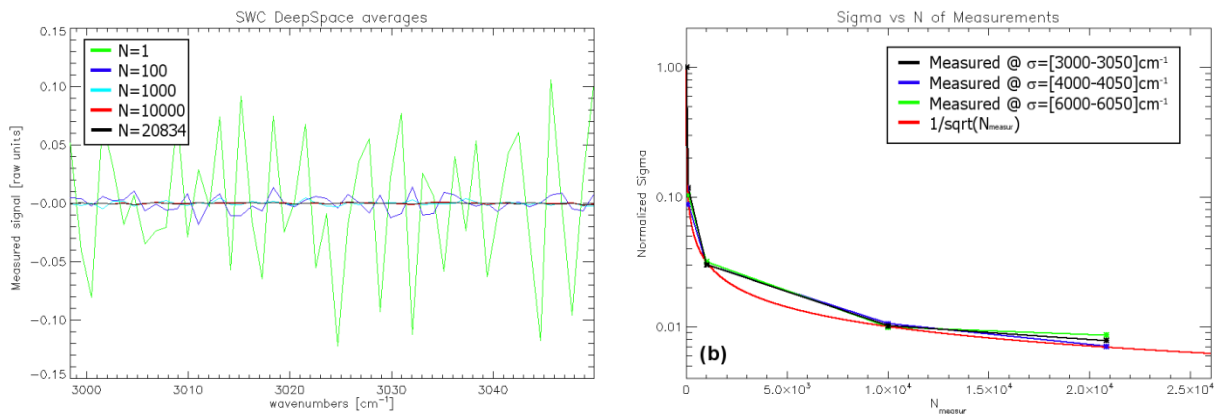
unapodized ILS is the responsible for the differences (“unidentified” spectral features) between the measured and synthetic spectra shown in **Fig. S2a**, and in previous CH₄ detections by PFS^{2,18}. In the current approach, this issue has been solved by (i) apply apodization to the measurements to reduce side lobes of the ILS and (ii) by improving the characterization of the apodized ILS.

Another important aspect of our new approach to CH₄ analysis is that, as described in step 3 below, we only consider relatively large averages of > 200 dayside spectra acquired in short time intervals (hours or minutes) and over a limited area, in order to increase the SNR and to account for the weak absorption, the relatively low abundance, and the high spatial and temporal variability of methane on Mars. Previous analyses of PFS data made use of relative small averages (~ 100 spectra^{2,18}), often collected in several weeks or months^{18,19}, resulting in a decrease of the SNR and of the quality of the spectral fit and, consequently, an increase of the uncertainties of the retrieved abundance.

Step 3: Ensemble averages and Spot-Tracking observations over Gale crater. The typical application of ensemble averages is found in Fourier-transform IR spectroscopy, where the final spectrum is the result of averaging hundreds of individual spectra. This is the only way to obtain a meaningful signal, when a single spectrum generates a practically unreadable signal heavily contaminated with random noise. Repetitive additions of noisy signals tend to emphasize their systematic characteristics and cancel out any zero-mean random noise. If SNR_o is the original signal-to-noise ratio of the signal, the final SNR_f after N repetitions is given by the following equation:

$$\text{SNR}_f = \text{SNR}_o \cdot \sqrt{N} \quad (\text{Eq. S1}).$$

As a consequence of **Eq. S1**, for a stable source and in the absence of systematic instrumental errors, the random noise is expected to decrease as $1/\sqrt{N}$, where N is the number of averaged spectra. We tested the validity of Eq. 1 for actual PFS measurements by collecting and averaging PFS observations of the deep space, a very stable source signal, where the expected level of the PFS measured signal is zero in the whole considered spectral range. The results are shown in **Fig. S4**.



Supplementary Figure S4: PFS random noise vs number of averaged spectra. (a) Raw PFS deep-space spectra in the relevant spectral range for methane. Single spectrum (green curve) is compared to ensemble averages of N=100 (blue), 1,000 (cyan), 10,000 (red) and 20,834 (black) spectra. (b) Normalized standard deviation of PFS deep-space spectra shown in (a) for different spectral intervals. The function $1/\sqrt{N}$ is also shown for comparison.

In agreement with **Eq. S1**, the measured standard deviation of PFS deep space spectra is inversely proportional to the square root of the number of averaged spectra N (**Fig. S4b**). This demonstrates that, in the considered spectral ranges, PFS is free of systematic instrumental errors and the ensemble average is an effective technique to increase the SNR in PFS average spectra.

The Mars Express spacecraft has been designed to perform several science pointing modes, including nadir pointing and spot pointing. The nadir pointing is carried out with a yaw correction to compensate for the rotation of Mars. Most of the PFS observations are acquired in nadir pointing. The spot-pointing mode is aimed at pointing the optical instruments to a surface feature on Mars and to track it. These observations are particularly suitable for methane retrievals because they allow acquisition of several hundreds of spectra over the same area and in a relatively short time period (typically a few tens of minutes). In **Table S1**, we summarize the list of spot-tracking observations over Gale crater performed by the PFS from December 2012 to July 2014, which roughly corresponds to the 20-month period of methane measurements at Gale Crater by Curiosity TLS-SAM⁴. Retrieved CH₄ abundance (column-integrated mixing ratio, MR, and column density, molec./cm⁻²) or upper limit (no direct detection, maximum abundance within 1- σ error bars) is also provided in the table, when applicable (i.e., more than 200 *dayside* spectra were collected by PFS in order to get sufficient SNR ratio for CH₄ retrieval).

Supplementary Table S1. List of spot-tracking observations over Gale crater performed by PFS-MEx from December 2012 to July 2014

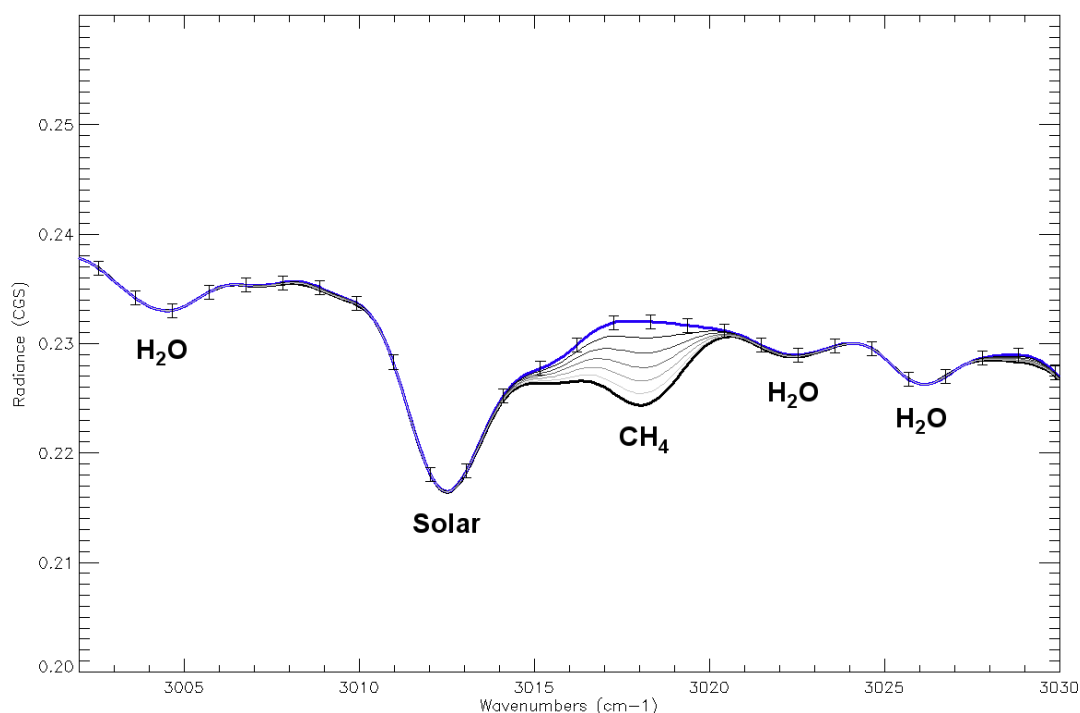
MEX Orbit	Date	Start Time (LT, hh.mm.ss)	Duration (minutes)	Retrieved MR ± 1 Sigma (ppbv)	Column Density ($\times 10^{15}$ molec./cm ⁻²)
11431_B	25/12/2012	10.19.45	40	N/A ^a	—
11613_B	16/02/2013	10.19.52	40	N/A	—
11919_A	16/05/2013	12.42.14	20	N/A	—
12025 ^b	16/06/2013	09.25.10	45	15.5 ± 2.5	4.07 ± 0.65
12029_B	17/06/2013	13.22.20	20	N/A	—
12032_B	18/06/2013	10.20.06	15	N/A	—
12781_B	22/01/2014	12.21.01	20	N/A	—
12816_A	01/02/2014	16.53.58	40	N/A	—
12876_B	19/02/2014	04.07.55	60	≤ 3.5	≤ 0.77
12904_B	27/02/2014	07.46.36	40	N/A	—
12985	22/03/2014	21.44.55	60	≤ 3.0	≤ 0.65
13006	29/03/2014	00.29.09	70	≤ 2.0	≤ 0.38
13017	01/04/2014	05.20.47	80	≤ 2.0	≤ 0.45
13052	11/04/2014	09.54.00	80	≤ 2.0	≤ 0.46
13140_A	07/05/2014	00.47.38	50	≤ 4.0	≤ 0.87
13140_B	07/05/2014	00.47.38	20	N/A	—
13154_B	11/05/2014	02.37.22	50	≤ 4.0	≤ 0.86
13154_C	11/05/2014	02.37.22	20	N/A	—
13207	26/05/2014	12.57.01	90	≤ 2.0	≤ 0.34
13221_B	30/05/2014	14.46.44	90	≤ 2.0	≤ 0.43
13309	25/06/2014	05.42.39	70	≤ 2.0	≤ 0.48
13397_B	20/07/2014	20.58.25	75	N/A	—

^aLess than 200 measurements or low-signal/nightside observations: not considered in the analysis

^bSolar Longitude $L_s = 336.6^\circ$

Averages of less than 200 measurements or low-signal/nightside observations are not considered in the analysis). Note that, for two different observations, the same value of retrieved MR does not necessarily correspond to the same value of the retrieved column density, due to the different atmospheric conditions (temperature and pressure profiles) in the observations. Methane is **only** detected in orbit 12025, performed on June 16, 2013. This date just follows martian sol 305 (after the landing of the Curiosity rover on June 15, 2013), when the Sample Analysis at Mars (SAM) instrument suite also reported elevated abundance of methane⁴.

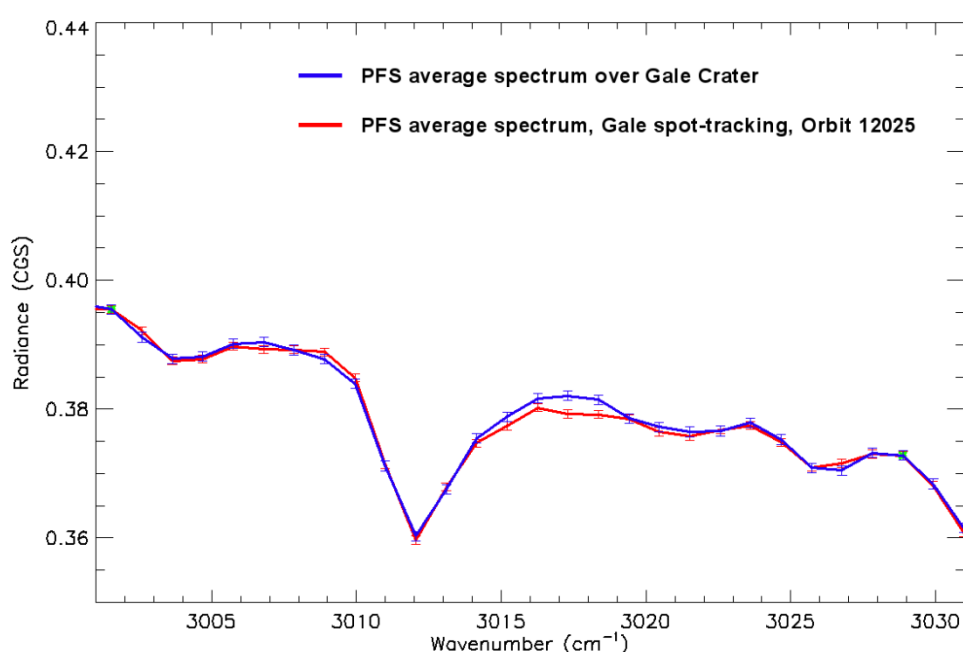
In order to evaluate the impact of the PFS data treatment described above to the retrieval of methane (e.g., sensitivity, upper limits), we calculated synthetic spectra for standard martian atmospheric conditions and applied the same treatment as for the real PFS spectra. The NESR of a single PFS spectrum at 3018 cm^{-1} is about $0.01\text{ erg/cm}^2\text{ s sr cm}^{-1}$ (CGS system of units; see ref.⁷⁸). As demonstrated in **Fig. S5**, our simulations show that, by applying the data treatment described in the three steps above, the averaging of 200 spectra (or more) will allow us to detect methane abundances as low as 5 ppbv (or less) even with apodized spectra. The zero-padding technique, an interpolation algorithm that increases the number of data points in the spectrum to improve the qualitative spectral features, has been applied to the synthetic spectra shown in **Fig. S5**. This algorithm is commonly used in Fourier spectroscopy⁸¹.



Supplementary Figure S5: Synthetic spectra different CH₄ abundances. Synthetic spectra calculated for standard atmospheric conditions and convoluted to the PFS apodized spectral resolution for different CH₄ abundances: 0 ppbv (thick blue), 10, 20, 30, 40, 50, and 60 ppbv (thick black). The H₂O mixing ratio is 300 ppm. 1- σ error bars (NESR) for co-addition of 200 measurements are also shown. Water vapor and solar lines are also indicated.

We also investigated the repeatability and the reliability of PFS measurements and of the observed spectral features, especially in the Gale crater area, after the implementation of the new data treatment described above. As an example, in **Fig. S6** we compare two independent PFS average spectra collected over Gale crater, one with a relatively strong methane absorption band and one without any CH₄-absorption feature. The first spectrum is an average of 280 measurements,

collected in spot-tracking mode during MEx orbit 12025 (**Table S1**). In this average spectrum, the CH₄ band is clearly visible (see main text). The second average is a collection of 200 nadir measurements performed over Gale crater in different martian years and seasons. In this second average spectrum, no CH₄ absorption feature is observed. Again, given the large spatial and temporal variability of methane on Mars, we did not expect to observe any CH₄ feature in this average since the individual spectra were selected at random and include various seasons and martian years. The two spectra were normalized to a same value in two spectral points (green spots in **Fig. S6**) to eliminate the effects of different geometry (mainly different illumination conditions), albedo (different areas observed within Gale crater), and suspended dust and ice opacity. The two spectra are very similar and their differences are within the 1- σ error bars everywhere except in the CH₄ absorption band centered at 3018 cm⁻¹ (**Fig. S6**). Apparently, the two average spectra also have similar water vapor abundance.



Supplementary Figure S6: Comparison PFS spectra with and without methane. Comparison of two independent PFS average spectra collected over Gale crater, with and without the methane absorption band. The red curve is an average of 280 measurements collected in spot-tracking mode during MEx orbit 12025 (**Table S1**); the blue spectrum is a collection of 200 nadir measurements performed over Gale crater in different martian years and seasons.

SI-2. Geological analysis

1. Where methane can be produced

Numerous hypotheses for the origin of methane on Mars have been proposed and challenged (summarized in refs^{16,17,24}). Among them, abiotic processes in subsurface rocks are considered as major candidates, including Fischer-Tropsch Type reactions using H₂ from serpentinization^{82,83} and from radiolysis⁸⁴, and thermogenesis of meteoritically delivered organics¹⁶. Such abiotic methane, along with any possible biotic methane, could be trapped in clathrates (e.g., ref.⁸⁵), zeolites and conventional reservoirs sealed by permafrost¹⁶. Fries et al.¹⁷ cast doubt that methane produced via serpentinization or biological activity could account for sudden plumes of martian methane (although this process has been widely observed on Earth¹⁶) and, as an alternative, they proposed that detected martian methane was produced by atmospheric UV-breakdown of carbonaceous material delivered into the martian atmosphere by periodic, cometary-origin meteor outbursts (or “meteor showers”).

However, Crismani et al.⁸⁶ suggested that even relatively small amounts of methane (e.g., a 10 ppbv plume) would require meteoritic material far in excess (by orders of magnitude) of any observed or predicted meteor fluences. Fries⁸⁷ counters that other data could support greater meteor infall and that occasional “meteor storms” on Mars might provide sufficient flux to account for the methane plumes.

Finally, there is no compelling evidence for a correlation between the atmospheric methane oscillations on Mars and predicted meteor streams⁸⁸, though Fries has noted that there could be reasons why such correlations may not be detected⁸⁹.

So, to date, the meteor hypothesis remains uncertain. Nevertheless, whether or not this hypothesis can account for some addition of methane to the martian atmosphere, there is a strong case that *subsurface* methane could have been produced on Mars by several processes (noted above)¹⁶. In this regard, Max et al.⁸⁵ conclude that the subsurface of Mars can be considered as a hydrocarbon province, with methane gas and hydrates occurring from depths of 1 m to 20 km, at least in the vicinity of the plumes reported by Mumma et al.³. Moreover, there are many processes known from terrestrial analogs that could trigger episodic emissions on Mars from these types of methane accumulations (e.g., destabilization of clathrates from temperature or pressure changes; breaching, melting or sublimation of permafrost seals; impacts or planetary stresses that produce new fractures, reactivate old fractures, and increase gas pressure along faults^{16,90}). Accordingly, we believe that sporadic releases from subsurface sources of methane are geologically likely on Mars and have focused this paper on that type of source for the contemporaneous methane detections by the PFS and Curiosity.

2. Where methane seepage can occur

On Earth, gas seepage systematically occurs in correspondence with faults, especially fault intersections, regardless the tectonic regime, either compressional (reverse and thrust faults), extensional (normal faults), uplift (radial faults) or shear (strike-slip faults) stress, and regardless fault activity and seismicity^{73,91,92}. Fault activity, which can be seismic or aseismic, may enhance gas migration processes, leading to more intense and episodic emissions, but it is not necessary for gas migration in general.

Published literature widely reports numerous examples of methane seepage in different types of faults and tectonic settings on Earth. Just to mention a few: seepage along normal faults occurs in the Katakolo Bay in Greece⁹³ and in the Tiber Delta in Italy⁹⁴; seepages along thrust faults are those typical (but not exclusive) of mud volcanoes worldwide^{75,92}. Giswil seep (Switzerland) is an

example of gas exhalation along a strike-slip fault⁹⁵. Gas migration studies demonstrate, then, that non-active, ancient faults in stable terrains (e.g., in granites, within cratons) can be gas-bearing (e.g., refs^{74,96}).

While compressional and extensional stresses may play a role in controlling liquid fluid (water and oil) migration (i.e. hydraulic conductivity), they do not significantly affect the gas-bearing property of faults (permeability to gas): a fault that is impermeable to water can be permeable to gas, as happens, for example, in argillaceous rocks and granites (e.g., refs⁹⁷⁻¹⁰⁰). Gas pressure is the main factor driving seepage even in poorly permeable and non-active (and non-seismic) fracture networks related to faults^{91,92}. Accordingly, by analogy, gas seepage on Mars may occur regardless the type of fault (tectonic regime) and seismic activity; microseepage may even occur along ancient faults, not active anymore. Detailed discussions are provided in ref.¹⁶.

3. *Evaluation of possible gas emission patterns, as input for the GCM simulations*

For the GCM simulations, we have considered realistic methane emission patterns (i.e., release intensity, duration, variation and area) described by Etiope and Oehler⁴² and based on gas seepage theory and experimental data acquired on Earth. For definition and description of the various “seepage” terms used here, the reader may refer, e.g. to refs^{39,69-76}). Gas emission from the ground to the atmosphere is basically considered an advective process, ruled by Darcy’s law, i.e. controlled by pressure gradients and permeability^{74,100,101}. Diffusion (ruled by Fick’s law) can be important only at depth, in low permeability rocks; modeling studies have actually suggested that diffusion cannot explain the methane plumes and concentration variations observed on Mars^{102,103}.

Flux intensity, duration and variation: On Earth, the intensity of methane emission (flux) from geological fluid manifestations may span a wide range of values, depending on the type of the seeping structure (gas-oil seep, mud volcano, microseepage from the soil), and specifically on the gas pressure and spatial extension (area) of the seep. Methane emission in active gas-oil seeps and mud volcanoes (bubbling pools, gas vents) is more or less constant over time but the flux may significantly change over short or long-time scales, depending on the variations of the subsurface gas pressure, which may be cyclic or irregular, and often induced by seismic activity (e.g., refs^{104,105}).

Methane emission from the diffuse microseepage (the slow, weak, areal exhalation of gas from the soil, without evident morphological features or fluid manifestations) is significantly controlled by exogenous (atmospheric and soil) factors, such as barometric pressure, wind intensity, soil temperature and humidity, and aquifer level. Microbial methanotrophic activity in the soil, modulated by soil temperature, humidity and organic content, determines seasonal variation of methane microseepage, which is higher in dry-winter periods, and lower in wet-summer periods. In a dry, water-free and, presumably, microbial-free ground condition such as that of Mars, possible seasonal (cyclic) variations of microseepage can only be related to seasonal variations of atmospheric factors (e.g., temperature, pressure, winds).

In permafrost regions, where methane of biological or geological origin, can be accumulated either within or below the permafrost layer, seasonal ice thawing produces summer increases of methane flux (e.g., ref.¹⁰⁶).

Methane release from single emission points (vents, macro-seeps) is typically in the order of 10^{-1} and 10^4 tonnes year⁻¹ (the flux from gas vents with a diameter <1 m is typically between 10^{-1} and 10^2 tonnes year⁻¹). Individual release events from focused seeps may emit orders of grams to several kg of gas in a few minutes (or tonnes of gas in mud volcano eruptions).

Diffuse exhalation from the ground (microseepage, over km² scale areas) is generally expressed in terms of grams per m² per day (typically mg m⁻² d⁻¹), and is frequently in the range

10^0 - 10^3 mg m⁻² d⁻¹. **Fig. S10** shows the range of values based on 1019 measurements from different sedimentary basins in North America, Europe and Asia (unpublished data-set derived from refs^{70,71,107-109}).

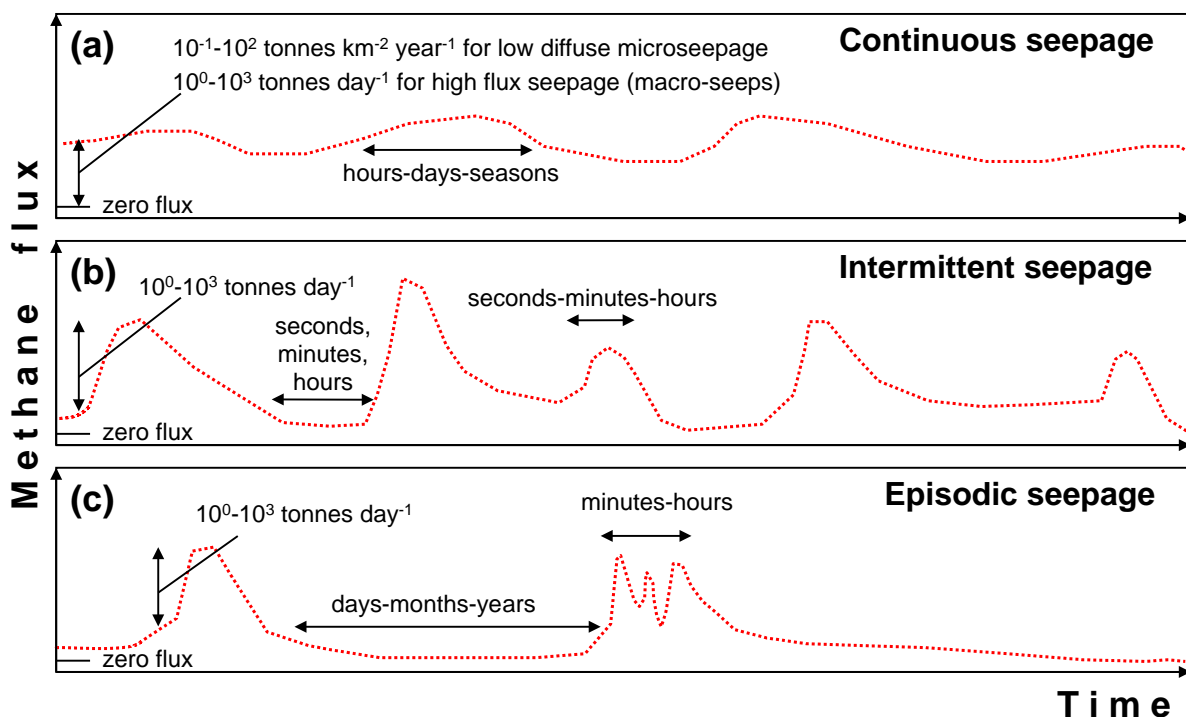
Following Etiope and Oehler⁴², the dynamics of gas emission from the ground can be summarized as follows (**Fig. S7**):

(a) continuous emission over long-term (years to geological time scale), with hourly, daily and seasonal weak oscillations (**Fig. S7a**); the emission refers to:

- high flux continuous venting (e.g., macro-seeps of hydrocarbons, active mud volcanoes hydrothermal-volcanic vents, mofettes, fumaroles);
- low flux diffuse microseepage: weak exhalations over wide areas and with lower oscillations.

(b) intermittent emission over long-term, with stronger and sudden, short-term (seconds, minutes, hours), variations, e.g. repeated gas eruptions, irregular venting in mud volcanoes and gas seeps, geysers. A continuous, background exhalation always accompanies this type of emission (**Fig. S7b**).

(c) episodic emission, with low or strong exhalations, spaced out by periods of days, months or years with very low or nil emission between the episodes. This pattern is typical of expulsion of gas pockets in shallow subsoil, driven by seismic activity or the Bernoulli effect induced by episodic strong winds and storms, or episodic migration of gas slugs along faults driven by seismic activity, overpressure pulses, and the so-called “fault burps”⁴². The events can be singular (one pulse) or multiple (sequence of sub-events), both lasting minutes or hours; generally, a weak continuous, background (quiescent) exhalation persists (**Fig. S7c**).



Supplementary Figure S7: CH₄ emission patterns. Main gas emission patterns observed in seepage phenomena on Earth (from ref.⁴²).

In all cases, gas seepage oscillations are modulated by either endogenous drivers (subsoil gas pressure build-up and discharges, rock permeability variations, ruptures of sealing rocks, upwelling of water controlled by hydrogeological factors) or exogenous drivers (barometric pressure changes, winds, tides).

On Mars, it is possible that episodic gas releases are also induced by meteoritic impacts, which may liberate gas trapped in shallow ground and permafrost or opening cracks that can act as preferential pathways for degassing⁹⁰.

It is important to consider that the “life time” of a seepage site is generally quite long or perennial, at least covering secular time-scales. Therefore, a site that may have episodically released methane on Mars, it expected to repeat the release soon or later.

Patterns (a) and (b) generally imply largest gas sources (and highly pressurized reservoir rocks). Since methane detections at the Gale crater have clearly had episodic character (ref.⁴ and this work), for the GCM simulations we assumed that methane release has been episodic (Type c in Fig. S7).

4. Geological context

On Mars, the dichotomy, separating the northern lowlands and southern highlands, is thought to reflect one of the oldest geologic events (possibly a major oblique impact) on the planet¹¹⁰. Because of the planet-wide size of this feature, faults associated with its formation are likely to have been deeply rooted. While some healing of such faults may be envisioned at great depth, continuing fault activity along the boundary is suggested by the presence at the martian surface of dichotomy-aligned scarps and troughs and associated erosion, and it has been suggested that the dichotomy has retreated southward through time from its initial position¹¹⁰. That continuing activity may be related to flexural stresses from differences in crustal thicknesses north and south of the boundary^{111,112}, relaxation of the dichotomy boundary by lower crustal flow¹¹¹³, global contraction, or local seismic events. Deep basement faults are always planes of weakness, and on Earth, such faults, even when ancient, are commonly reactivated by subsequent stresses and exert long-lived controls on development of overlying features (e.g., ref.¹¹⁴). So, on Mars, dichotomy faults have potential to provide conduits for both liquid and gas migration from depth and may tap materials from basins associated with adjacent large craters and from some of the deep basins in the northern plains.

Gale crater is the largest mid-sized crater on the dichotomy. The north western sector of the crater has been investigated by Curiosity and is characterized by fractured terrain, including abundant calcium sulfate-filled fractures¹¹⁵ and extensive polygonal boxwork ridges interpreted as early diagenetic features, formed in a phreatic zone saturated with water; accordingly, the crater has been suggested to have been a site of substantial, early diagenetic groundwater influx¹¹⁶. Consistent with that view is the work of refs^{117,118}, who have modelled precipitation-induced aquifer recharge that may have affected Gale. These authors have used hydraulic head and flow vectors that converge into Gale crater to suggest that Gale was a deep sink in its part of the dichotomy during the late Noachian when the planet was starting to dry from a previous, relatively wet period^{117,118}. This along with the study of ref.¹¹⁶ implies deep groundwater influx into Gale early in its history that potentially could have included methane from deep sources.

The dichotomy east of Gale is an area of fretted terrain called Aeolis Mensae. Aeolis Mensae is a complex region of Noachian-Hesperian hills, plateaus and grabens with multiple extensional faults and fault intersections that could act as release zones for methane from depth.

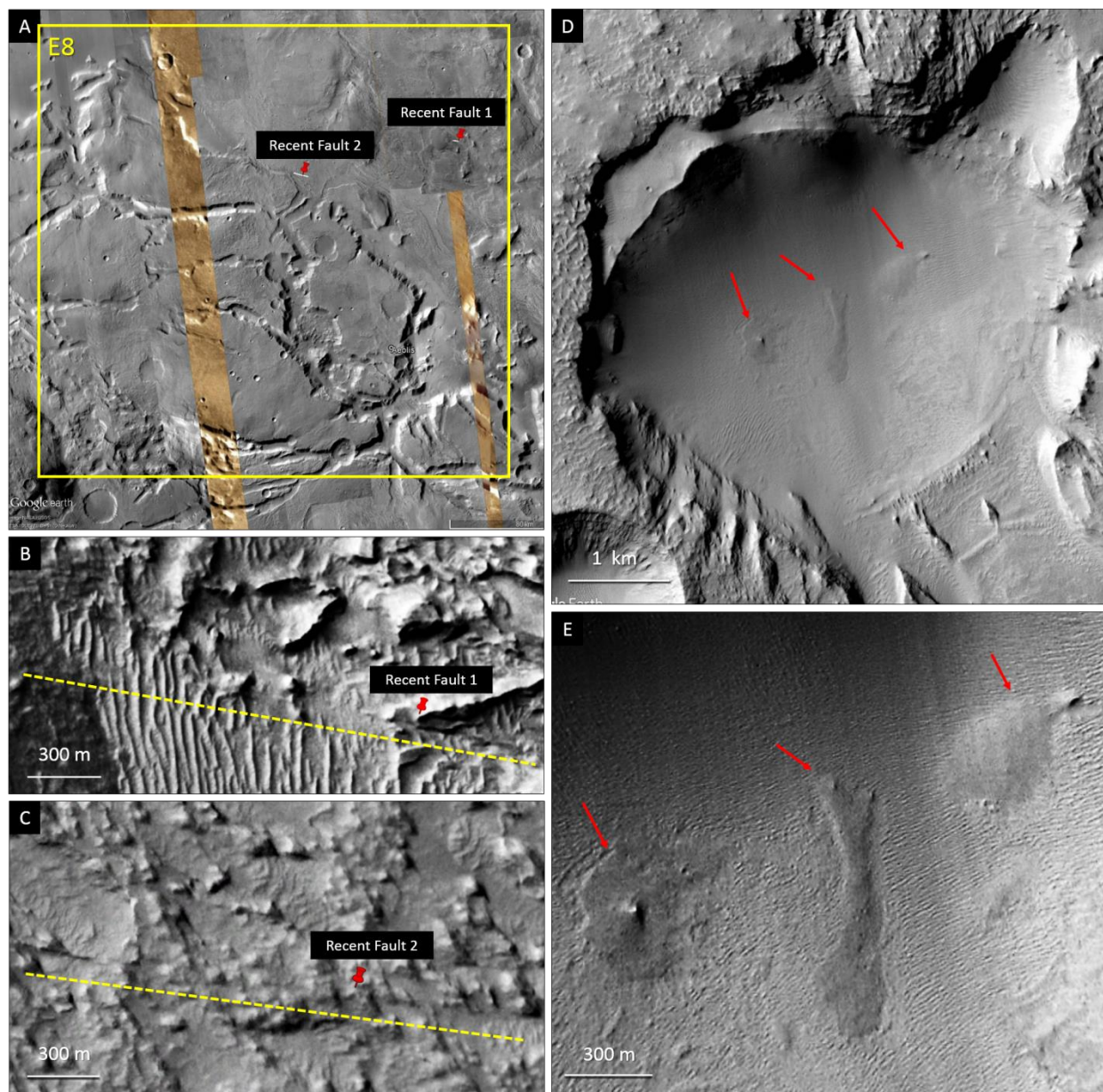
While similar fretted terrain along the dichotomy at mid latitudes has been attributed to the effects of Amazonian ice modification^{119,120}, the fretted terrain of equatorial Aeolis Mensae appears to lack the lineated valley fill and lobate debris aprons that are characteristic of Amazonian glacial deposits¹¹⁹, and work by ref.¹²¹ suggests that Aeolis Mensae may represent a site of Hesperian

glaciation. Accordingly, it is not clear whether fractures associated with Aeolis Mensae are deep faults associated with the dichotomy or if they are more shallow features associated with glaciation. Nevertheless, even if the fractures of Aeolis Mensae are shallow features, being located on the dichotomy, they could connect with the deeply-rooted dichotomy faults that may tap liquids and gases from depth. And as discussed above, any fault system can, in theory, be a potential site of methane release. Based on the map of ref.³⁹, faults are mainly distributed along grid blocks associated with the dichotomy, though fault density appears to be highest in the eastern blocks (also **Fig. 2**, main text).

Within the eastern section of the grid are the westernmost lobes of the lower member of the Medusae Fossae Formation (MFF), a volcanoclastic deposit of Hesperian to Amazonian age⁴³. New analyses of neutron spectrometer data from Mars Odyssey⁴⁴ suggest that bulk ice may be present in the uppermost meter of those western MFF lobes (**Fig. 4**, main text). Since ice today is unstable in equatorial regions on Mars, this shallow ice may reflect past times of high obliquity⁴⁴ or it might signal recent input from deep conduits that tap liquid water (such as deep faults along the dichotomy, noted above). The latter possibility could reflect processes similar to those responsible for the recent flooding in Athabasca Valles (suggested to be sourced from deep regional aquifers or a deep global groundwater table¹²²). In such scenarios, methane of deep origin may be transported by the groundwater, or it may follow the same migration pathway, to the surface. Since outcrops of Aeolis Mensae appear to be present within the MFF (**Fig. 4**, main text), it is likely that Aeolis Mensae and its faults/fractures underlie the MFF. As noted in the main text, we suspect that these faults have penetrated ice in the MFF. This is based on evidence that the faults have continued to be reactivated by ongoing planetary stresses, as we have identified lineations (likely faults) in Block E8 offsetting relatively young dunes and yardangs in the MFF (**Fig. S8 A-C**); those lineations have orientations similar to those of major faults in Aeolis Mensae and may reflect recent movement of Aeolis Mensae faults buried below the cover of the MFF. These lineations extend into the area where ref.⁴⁴ have predicted shallow ice. Accordingly, we have suggested the possibility that bulk ice in the MFF may seal subsurface methane but that such methane could be released episodically along faults that penetrate the ice. In addition, we are continuing to investigate unusual flow-like structures in Block ESE (**Fig. S8 D-E**) to determine whether they might be release structures for methane. HiRISE images are not yet available, but new image acquisitions may help in future interpretations of those structures.

Blocks E8, ESE and ESEE were discussed in some detail in the main text. Here we discuss the remaining blocks of the grid, as these appear to be of lesser merit. Block ENE only includes a single, minor outcrop of Aeolis Mensae (**Fig. 4**), perhaps suggesting that Aeolis Mensae may be deeper in Block ENE than in Block E8. For Block E12, only its far SW corner is close to the present-day dichotomy and that location is far from the mapped bulk ice.

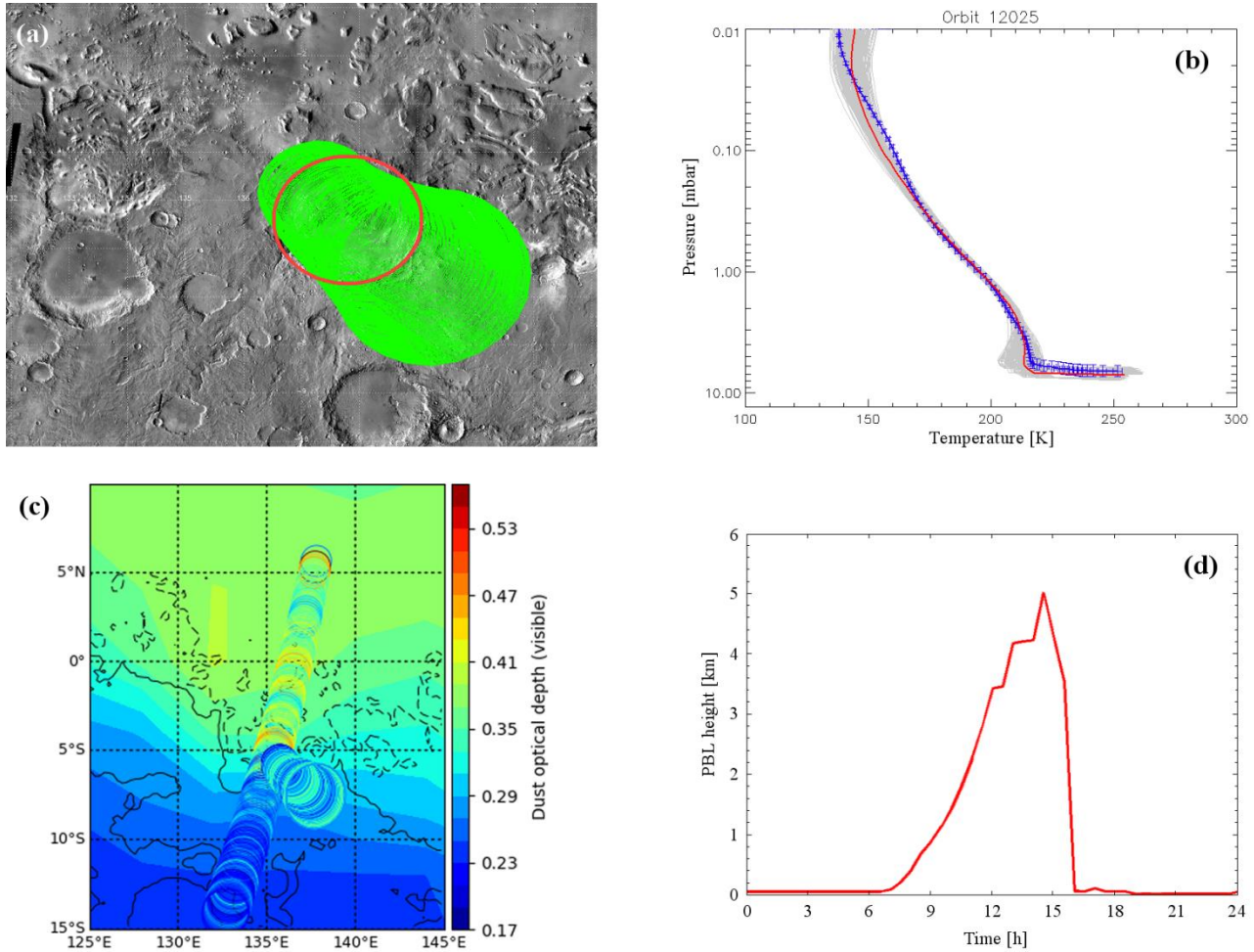
All other blocks of the grid would seem to have lower potential for gas seepage. Among the eastern and most northerly blocks, E4, NE4, N8, NNE, NE8 and NE8E are much farther from the bulk ice, and NE4, NNE, NE8, NE8E, and ENEE are far from the present-day dichotomy. Blocks NNE, NE8, and ENE have aligned knobs (**Fig. 4**) which were interpreted as pseudocraters (rootless cones) with possible hydrothermal input⁴⁵ or features associated with magmatic eruptions from fissures⁴⁶. If shallow rootless pseudocraters, the knobs would lack a conduit for deep upwelling fluids; if sites of magmatism, they could emit methane, but, by analogy with sediment-free magmatic emissions on Earth, their methane content could be quite low^{16,90}. The blocks containing Gale crater (G, E4, S4, SE4), as well as the remaining blocks south and west of Gale, are quite distant from the shallow ice in the MFF, and although there are certainly faults associated with Gale and other craters in those regions as well as with the dichotomy within and west of Gale, we did not detect any evidence of fractured, fretted terrain comparable to that of Aeolis Mensae or other types of structures (such as mud volcanoes) likely to represent release points for methane in these blocks.



Supplementary Figure S8: Lineations and flow-like structures in Blocks E8 and ESE. (A-C), lineations in Block E8: (A), location in block; (B-C), extent and orientation (indicated by dashed lines plotted just south of the lineations). (D-E), flow-like structures in a crater at 6.66°S, 144.5°E in Block ESE: (D), crater view; (E), details. All images from Google Earth CTX camera image mosaics. (A) includes Visible Image data where CTX data not available. North is up in all panels.

SI-3. Where the emission detected by PFS and TLS took place

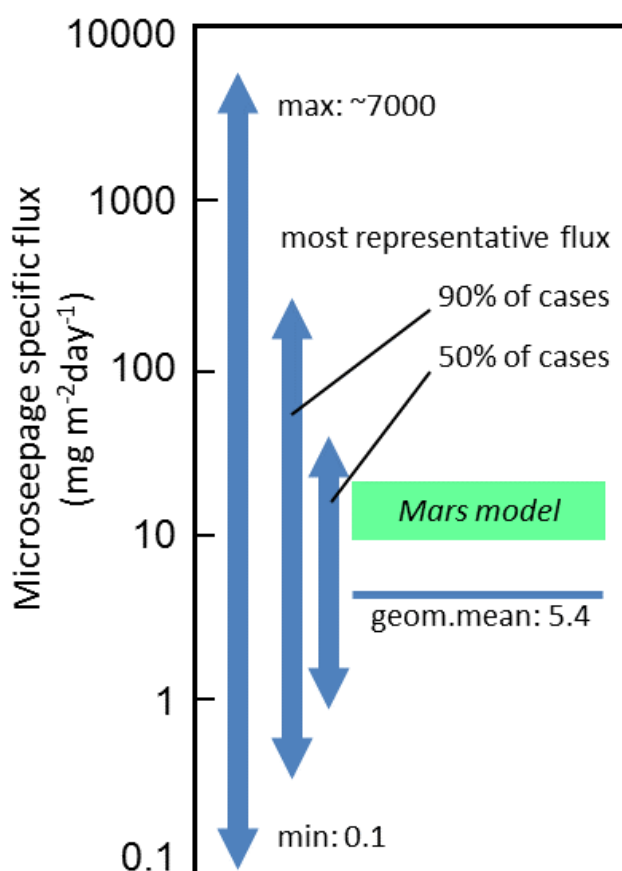
The detection (ingestion) of methane by Curiosity on Sol 305 was performed at ~13:00 while the convective cells in the planetary boundary layer (PBL) were being developed. Above the crater's rim (~2 – 4.5 km), the methane would be advected outside of the crater. The PBL reached a maximum height of ~5 km at ~15:00 before collapsing rapidly one hour later (see **Fig. S9d**).



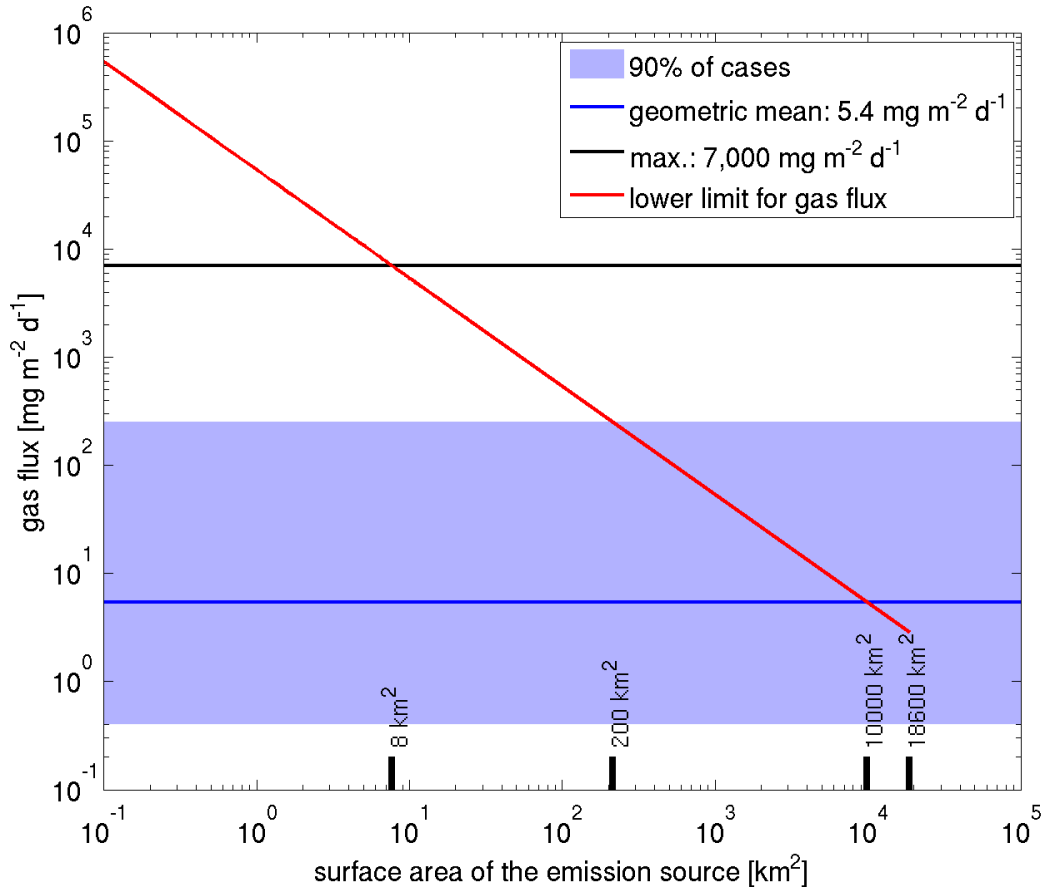
Supplementary Figure S9: PFS observations and GCM simulations at Gale. (a) Footprints (green ellipses) of PFS spot-tracking observations in orbit 12025. Background image from THEMIS Day IR Global Mosaic maps (http://www.mars.asu.edu/data/thm_dir/). Red ellipse marks the rim of Gale crater. (b) Atmospheric temperature profiles retrieved by PFS LWC for the same orbit (grey curves). The average profile used for the calculation of synthetic spectra is shown in red (see Methods). The blue curve is the average temperature profile over Gale crater simulated in the GEM-Mars GCM at the time of the PFS observation, see Methods. (c) Dust optical depth on sol 306: comparison between GEM-Mars (background) and PFS measurements (circles). See Methods. (d) Height of the planetary boundary layer (PBL) simulated in GEM-Mars at $L_s = 336^\circ$ at the closest model grid point ($4^\circ\text{S}/136^\circ\text{E}$) to Gale crater.

If the emission took place *within* the crater, most of the methane detected by PFS must then have been emitted in the 17.5-hour time window between the collapse of the PBL at ~16:00 on sol 305 and the PFS observation. This corresponds to a *minimal* gas flux of 53 tonnes day⁻¹. This level of gas output can result from a focused, point-source type of seep (such as that from a vent or a mud volcano) or from a diffuse microseepage over a relatively large area. If methane were released from

a point source, the emission of 53 tonnes day⁻¹, with its eruptive character (it would last no longer than 17.5 hours), could occur only from large mud volcanoes (such as those in Azerbaijan⁹⁰) or very active large gas seeps (not related to mud volcanism; see also SI-2). Such features have not been identified in Gale crater to date. Alternatively, for diffuse microseepage, typical fluxes on Earth are in the order of 1-100 mg m⁻² day⁻¹, with a geometric mean of about 5 mg m⁻² day⁻¹ (see SI-2 and **Fig. S10**). Assuming this mean value for Gale crater, the minimum release area would be ~10,000 km², i.e. more than 50% of the entire crater area. That is not very likely. For higher microseepage fluxes (on the order of 10²-10⁴ mg m⁻² day⁻¹), the degassing areas could be smaller: a few hundred to ~5 km² (**Fig. S11**). But by analogy with terrestrial analogues⁹⁰, such an intense microseepage would imply the existence of pressurized gas reservoirs coupled with permeable fracture and fault systems. For this high level of flux, degassing would typically be less episodic and enhanced methane abundance should have been detected more frequently by TLS-SAM and the PFS.

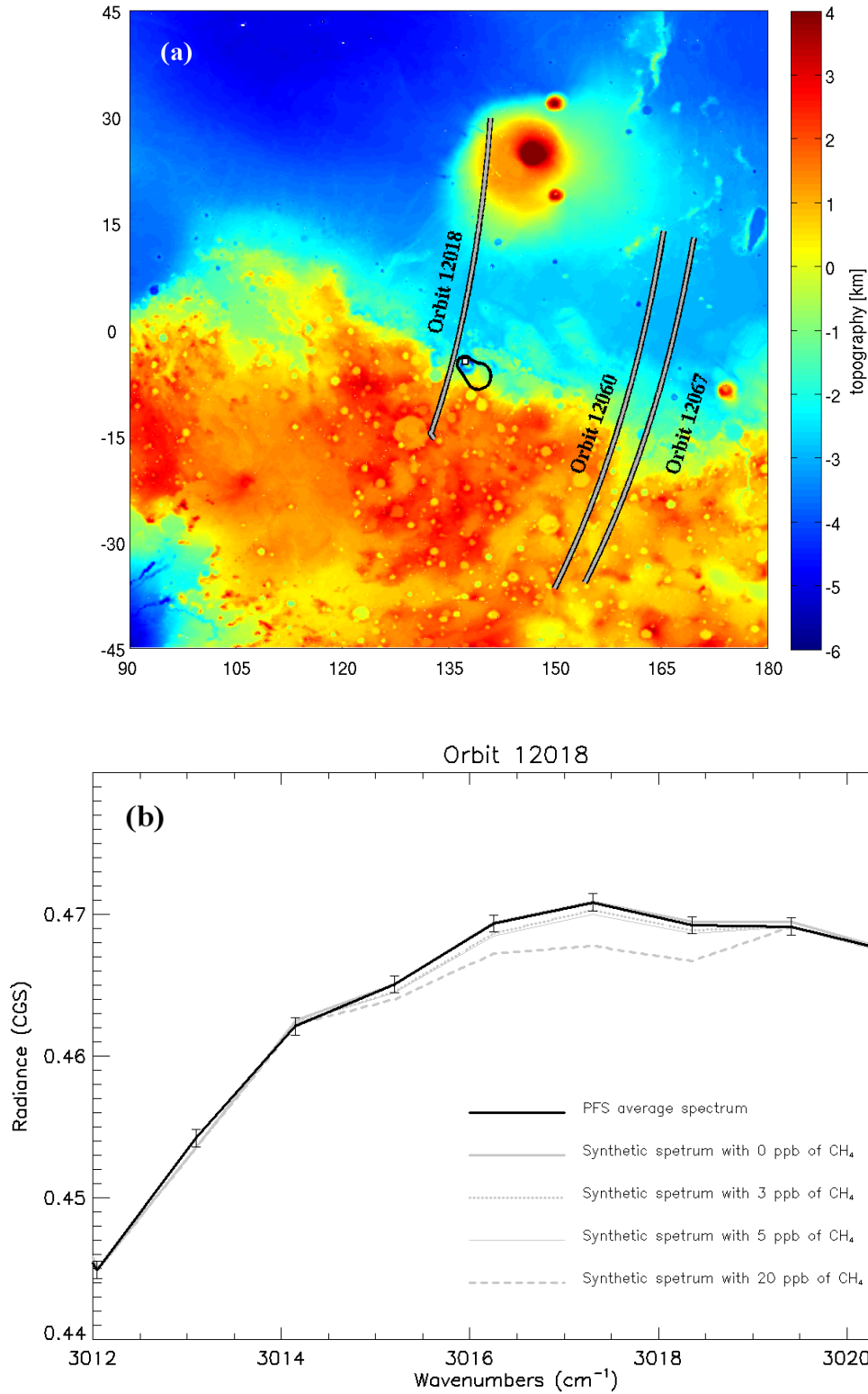


Supplementary Figure S10: Microseepage flux rates on Earth and release rate on Mars. Comparison between methane microseepage flux rates on Earth (blue) and modelled release rate on Mars (green) obtained in 95% of release scenarios from grid Block E8. Microseepage (mg m⁻² day⁻¹) range and geometric mean are based on a dataset of 1019 measurements from different sedimentary basins in North America, Europe and Asia (unpublished data-set described in **SI-3**). The modelled emission scenarios on Mars are consistent with the most common terrestrial microseepage. For the 4°×4° horizontal resolution of the area, the overall CH₄ output is equivalent to the seepage observable on Earth from a relatively small sedimentary basin (order of 10⁶ kg day⁻¹, over about 56,000 km²).



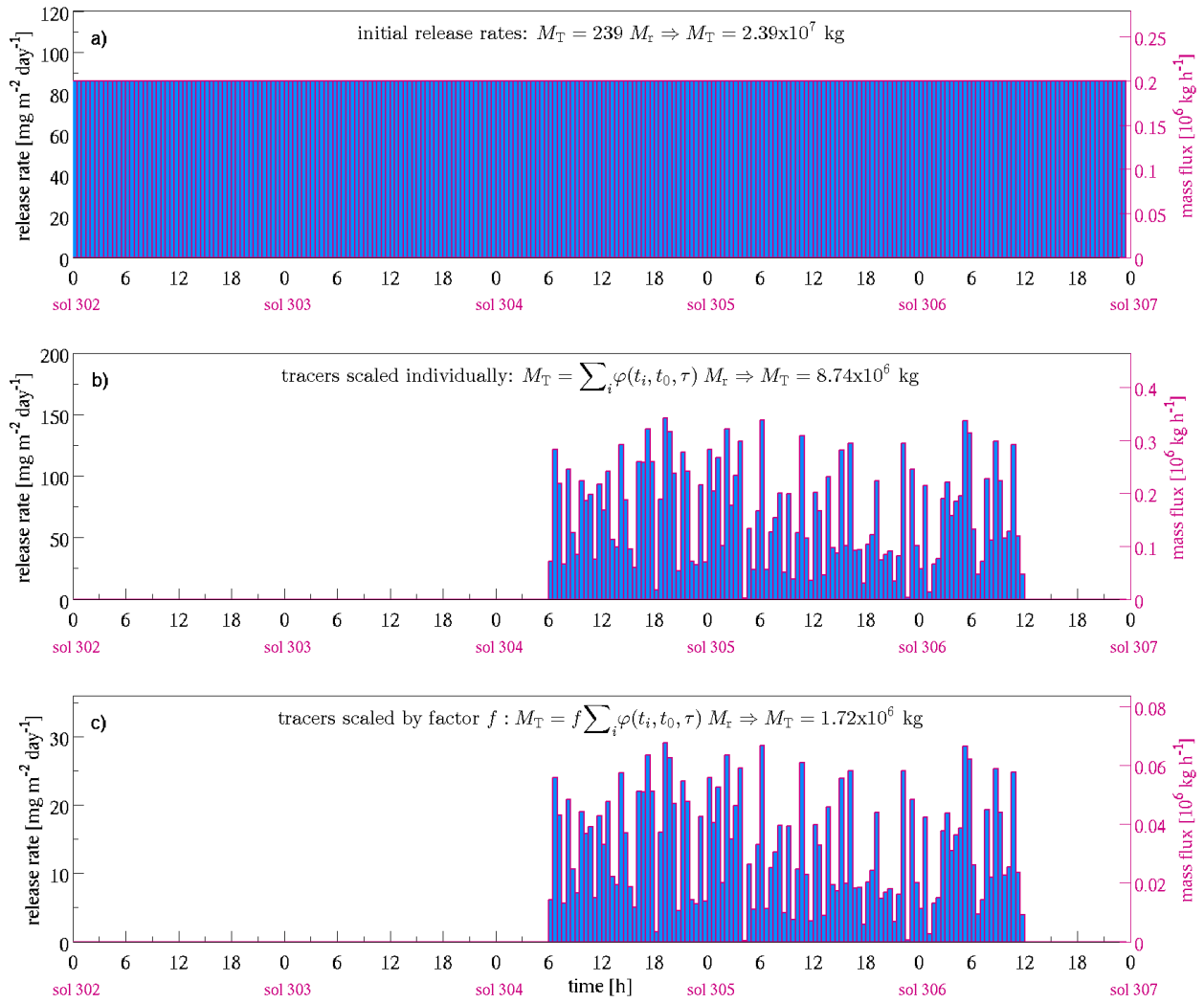
Supplementary Figure S11: Mean gas flux vs surface areas Lower limit for the mean gas flux (red line) required to observe a release of 39 tonnes over 17.5h for a large range of surface areas. The maximum surface area is $\sim 18,600 \text{ km}^2$ (i.e. the total surface area of the crater). Comparison is done with statistical measurement data of microseepage recorded on Earth (see also **Fig. S10**). The highest microseepage CH_4 fluxes measured on Earth (black line) are in the order of $\sim 7,000 \text{ mg m}^{-2} \text{ d}^{-1}$. The blue area indicates the range of fluxes in 90% of cases observed on Earth.

If the gas emission took place *outside* the crater, release through diffuse microseepage over a wide area and/or through faults could easily account for the methane flux suggested by the PFS detection (see SI-2 and below for details). Moreover, the methane could be advected towards Gale crater, where it would mix down to the surface because, at this time of the year, the PBL height exceeds the crater rim for a few hours per day (**Fig. S9d**). For a distant source, the plausibility of being a source location for the observed event also highly depends on the meteorological conditions. In the absence of wind measurements on Mars, atmospheric models can provide a first indication about the transport of methane. Upon a surface release, methane would be rapidly (within a few hours) transported up to the top of the planetary boundary layer (PBL) at $\sim 5 \text{ km}$ where it would be picked up by the global circulation patterns²⁸. The source could be at a distance from Gale that is outside of the central domains of mesoscale models^{91,123}. While a mesoscale model would be capable of resolving the fine-scale wind patterns in the crater, a GCM can provide an estimate of the larger-scale circulation patterns in the wider area around the crater. The footprint of the PFS spot-tracking observation (**Fig. 2**) has an area comparable to that of a GCM grid cell but is much larger than the central domains of mesoscale models, and the additional PFS orbits that form important constraints reach outside of the mesoscale domains (**Fig. S12a**).

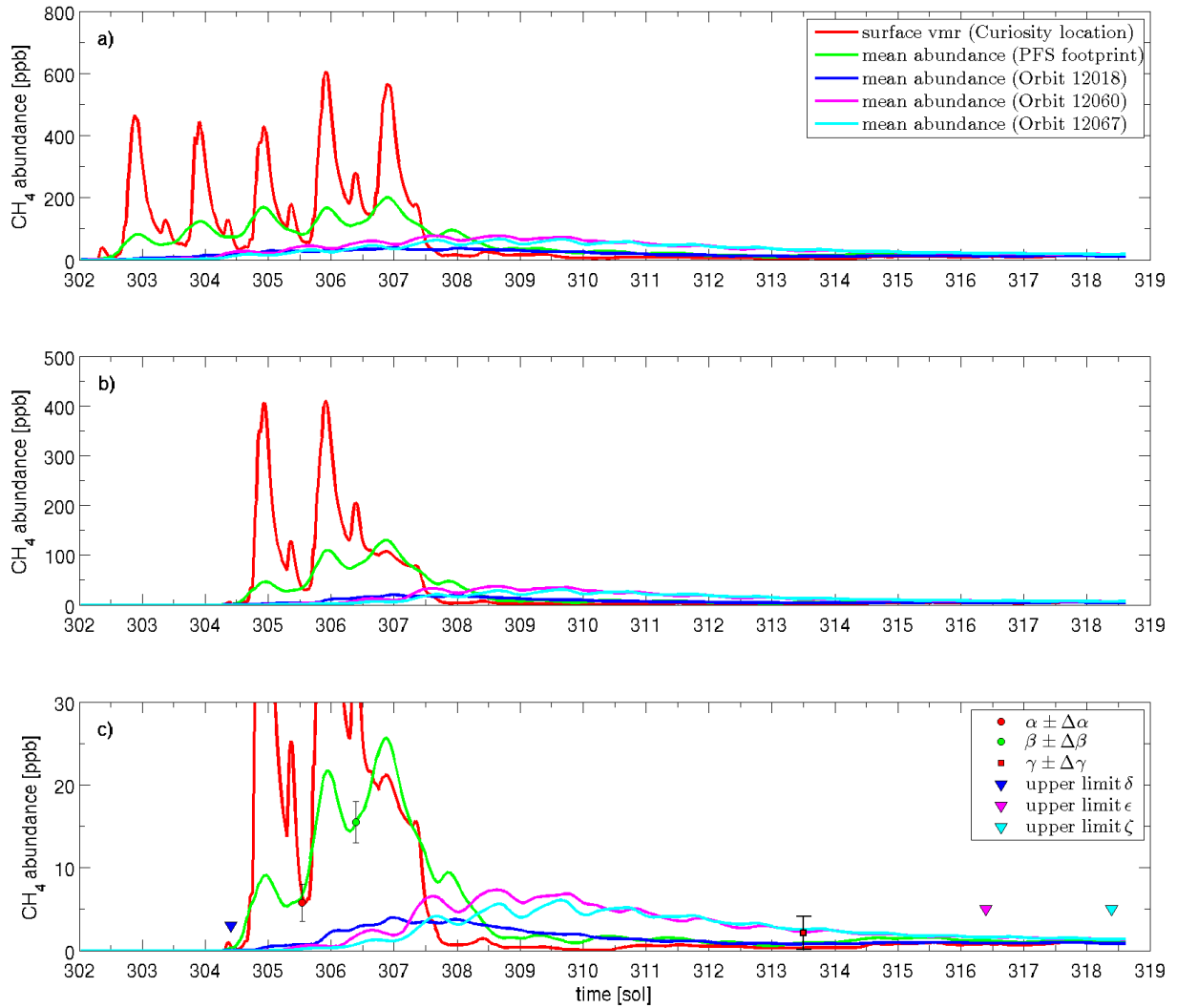


Supplementary Figure S12: PFS orbit tracks and example of CH₄ upper limit retrieval. Observational constraints. (a) Topography (MOLA) in the region surrounding Gale crater. The rover's location is indicated with a white marker. The black curve delimits the area of PFS observations on Sol 306. The lines in grey show the tracks of the PFS orbits included in the model study as additional observational constraints (see **Table 1**). (b) Methane upper limit in PFS orbit 12018. The PFS average spectrum (thick black curve, average of 276 spectra) is compared to synthetic best-fit spectra with various CH₄ abundance (grey curves): 0 ppbv (thick), 3 ppbv (dotted), 5 ppbv (thin), and 20 ppbv (dashed). 1-σ error bars are also shown.

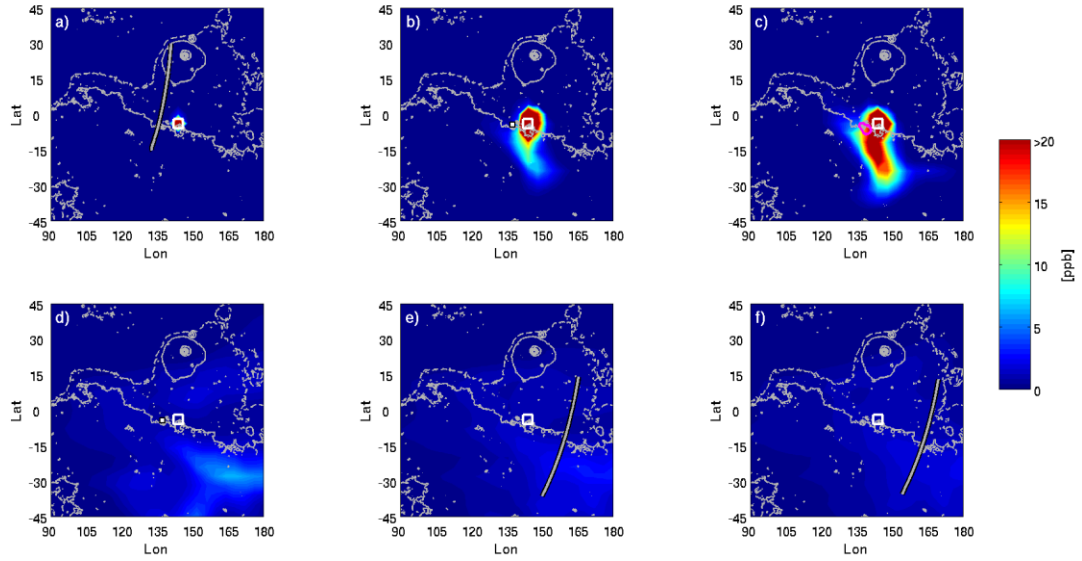
Additional Supplementary Figures



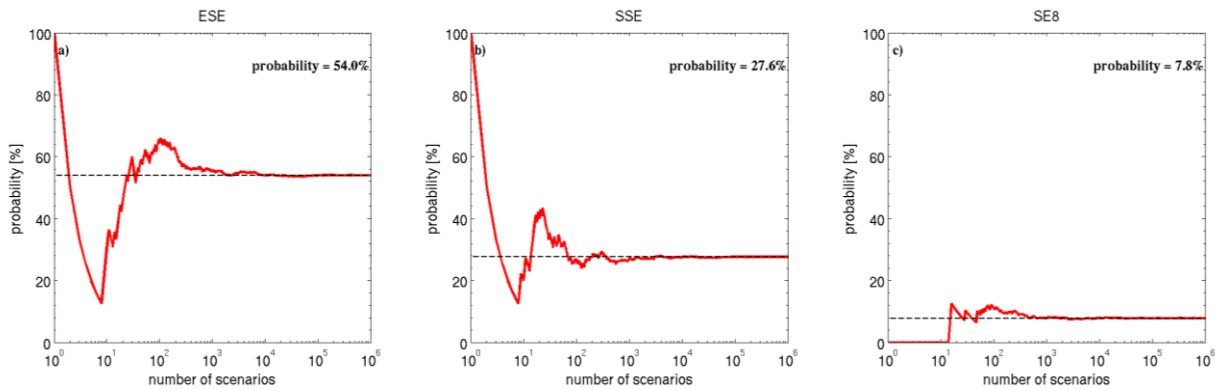
Supplementary Figure S13: Illustration of the procedure followed to produce one release pattern. a) combination of the full set of tracers as they are released in the numerical experiments; b) emission pattern after the tracers are individually scaled by factors $\varphi_i(t_i, t_0, \tau)$ generated using a uniform probability distribution function; c) final release pattern after every tracer is scaled by the same factor f . In this example, the emission event starts on Sol 304 at 6 a.m. ($t_0 = 54$ h) and lasts 2 sols, 5 hours, 30 minutes ($\tau = 53.5$ h).



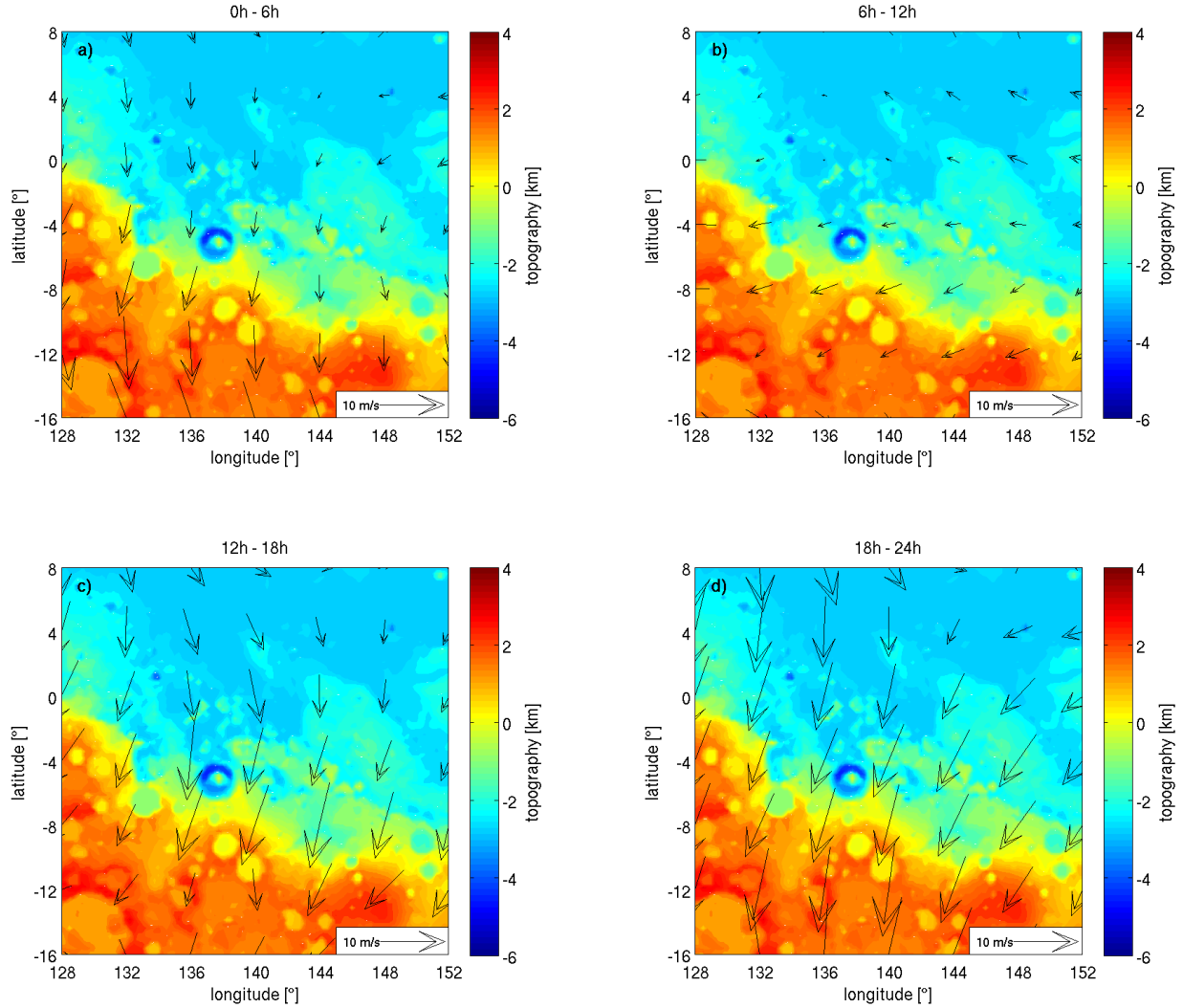
Supplementary Figure S14: Example of CH_4 time evolution. Time evolution of the surface volume mixing ratio at the rover's location, and of the vertically-integrated abundance measured by PFS in the 3-step procedure described above. The final result shown in the bottom figure illustrates a release scenario (Block E8 in this example) consistent with all available observational constraints described in the legend.



Supplementary Figure S15: Example of CH₄ spatial distribution at the time of observations. Methane abundance (column-averaged mixing ratio) in the release scenario from E8 shown in Figs. S13 and S14. The maps correspond to the times of the respective observations (Tables 1 and 2): (a) PFS orbit 12018 (sol 304), (b) TLS-SAM detection (sol 305), (c) PFS orbit 12025 (spot-tracking, sol 306), (d) TLS-SAM detection (sol 313), (e) PFS orbit 12060 (sol 316), (f) PFS orbit 12057 (sol 318). The PFS orbits are indicated in grey. The emission site and the MSL location are indicated with a rectangle and a white square, respectively.



Supplementary Figure S16: Probability of fitting the observations as a function of the number of scenarios. The probability is given by the number of scenarios consistent with the observations divided by the size of the sample. Three emission sites are considered: a) ESE, b) SSE, and c) SE8.



Supplementary Figure S17: atmospheric circulation around Gale. Horizontal winds around $L_s = 336^\circ$ and averaged below 5 km and in four periods of time: a) 0h – 6h; b) 6h – 12h; c) 12h – 18h; d) 18h – 24h. As the emission event occurred over a relatively short period of time, most of the methane was still in the boundary layer at the time of the detections by MSL and PFS. This figure shows the atmospheric circulation below 5 km in the region surrounding Gale crater around $L_s = 336^\circ$. The horizontal winds are southwards most of the time, except in the morning (panel b) where they are westwards. As a result, any plume of methane originating from the east of Gale crater moves essentially to the south. However, given the wind direction in the morning, the plume is gradually spread to the west. This is illustrated in Fig. S15.

References

77. Davis, S. P., Abrams, M. C. & Brault, J. W., *Fourier Transform Spectrometry*, Academic Press (2001).
78. Giuranna, M., et al., Calibration of the Planetary Fourier Spectrometer short wavelength channel. *Planet. Space Sci.* **53** (10), 975–991 (2005).
79. Naylor, D.A. & Tahic, M. K., Apodizing functions for Fourier transform spectroscopy. *J. Opt. Soc. Am. A* **24**, 3644–3648 (2007).
80. Poulin, R., Dutil, Y., Lantagne, S. & Châteauneuf, F., Characterisation of the ACE-FTS instrument line shape. *Proceedings of SPIE Vol. 5151 Earth Observing Systems VIII*, edited by William L. Barnes (2003).
81. Bell, R.J., *Introductory Fourier Transform Spectroscopy*, Academic Press, New York (1972).
82. Ehlmann, B.L., Mustard, J.F. & Murchie, S.L. Geologic setting of serpentine deposits on Mars. *Geophys. Res. Lett.* **37** (2010).
83. Mustard, J.F. & Tarnas, J.D. Hydrogen production from the upper 15 km of martian crust via serpentinization: implications for habitability. 48th Lunar and Planetary Science Conference, Abs. # 2384 (2017).
84. Tarnas, J. D., Mustard, J. F., Sherwood Lollar, B., Bramble, M. S., Cannon, K. M., Palumbo, A. M. & Plesa, A.-C. Radiolytic H₂ production on Maachian Mars: Implications for habitability and atmospheric warming. *Earth Planet. Sci. Lett.* **502**, 133–145 (2018).
85. Max, M. D., Clifford, S. M. & Johnson, A. H. Hydrocarbon system analysis for methane hydrate exploration on Mars, in W. A. Ambrose, J. F. Reilly II, D. C. Peters, eds., *Energy resources for human settlement in the solar system and Earth's future in space: AAPG Memoir* 101, 99–114 (2013).
86. Crismani, M.M.J., Schneider, N.M. & Plane, J.M.C. Comment on “A cometary origin for atmospheric martian methane” by Fries et al.,. *Geochem. Persp. Lett.* **3**, (2017). doi:10.7185/geochemlet.1715
87. Fries, M. (2017). Reply to Comment on “A cometary origin for martian atmospheric methane” by Crismani et al. *Geochem. Persp. Lett.* **3** (2017). doi: 10.7185/geochemlet.1716
88. Roos-Serote, M., Atreya, S.K., Webster, C.R. & Mahaffy, P.R. Cometary origin of atmospheric methane variations on Mars unlikely. *J. Geophys Res: Planets* **121**, 2108–2119 (2016).
89. Fries, M. Comment on “Cometary origin of atmospheric methane variations on Mars unlikely” by Roos-Serote et al. 2016. *JGR Planets* 122 (4), 784–786.
90. Etiope, G., Natural gas seepage. *The Earth's Hydrocarbon Degassing*. Springer, Cham, Switzerland, pp. 199 (2015). doi:10.1007/978-3-319-14601-0
91. Pla-Garcia, J., et al., The meteorology of Gale crater as determined from rover environmental monitoring station observations and numerical modeling. Part I: Comparison of model simulations with observations. *Icarus* **280**, 103–113 (2016).
92. Bonini, C. Fluid seepage variability across the external Northern Apennines (Italy): structural controls with seismotectonic and geodynamic implications. *Tectonophysics* **590**, 151–174 (2013).
93. Etiope, G., et al., Offshore and onshore seepage of thermogenic gas at Katakolo Bay (Western Greece). *Chem. Geol.* **339**, 115–126 (2013).

94. Ciotoli, G., et al. Tiber delta CO₂-CH₄ degassing: a possible hybrid, tectonically active Sediment-Hosted Geothermal System near Rome. *J. Geophys. Res. - Solid Earth* **121**, 48–69 (2016).
95. Etiope, G., et al., Origin and flux of a gas seep in the Northern Alps (Giswil, Switzerland). *Geofluids*, **10**, 476–485 (2010).
96. Malmqvist, L., & Kristiansson, K., Experimental evidence for an ascending microflow of geogas in the ground. *Earth Planet. Sci. Lett.* **70**, 407–416 (1984).
97. Etiope, G., & Lombardi, S., Evidence for radon transport by carrier gas through faulted clays in Italy. *J. Radioanalyt. Nucl. Chem.* **193**, 291–300 (1995).
98. Horseman, S.T., Harrington, J.F., & Sellin, P., Gas migration in clay barriers. *Eng. Geol.* **54**, 139–143 (1999).
99. Ciotoli G., et al. Migration & behaviour of gas injected into a fault in low-permeability ground. *Quart.J.Eng..Geol.and Hydrog.*, **38**, 305–320 (2005).
100. Etiope, G. & Martinelli, G., Migration of carrier and trace gases in the geosphere: an overview. *Phys Earth Plan. Int.* **129**, 185–204 (2002).
101. Brown, A., Evaluation of possible gas microseepage mechanisms. *Am Assoc Pet Geol Bull* **84**, 1775–1789 (2000).
102. Stevens, A., Patel, M.R., & Lewis, S.R., Numerical modelling of the transport of trace gases including methane in the subsurface of Mars. *Icarus* **250**, 587–594 (2015).
103. Stevens, A.H., Patel, M.R., & Lewis, S.R., Modelled isotopic fractionation and transient diffusive release of methane from potential subsurface sources on Mars. *Icarus* **281**, 240–247 (2017).
104. Delisle G., et al., First approach in quantifying fluctuating gas emissions of methane and radon from mud volcanoes in Azerbaijan. In Wood L. ed., *Mobile shale basins*. AAPG Memoir 93, 211–224 (2010).
105. Yang T.F., et al., Seismo-geochemical variations in SW Taiwan: multi-parameter automatic gas monitoring results. *Pre Appl. Geoph.* **163**, 693–709 (2006).
106. Christensen, T.R., et al., Thawing sub-arctic permafrost: Effects on vegetation and methane emissions. *Geophys. Res. Lett.* **31**, L04501 (2004). doi:10.1029/2003GL018680.
107. LTE, Inc., Phase II Raton basin gas seep investigation las animas and huerfano counties, Colorado, Project #1925 oil and gas conservation response fund (2007).
108. Sciarra A., et al., Geochemistry of shallow aquifers and soil gas surveys in a feasibility study at the Rivara natural gas storage site (Po Plain, Northern Italy). *Appl. Geochem.* **34**, 3–22 (2013).
109. Tang, J., et al., Microseepage of methane to the atmosphere from the Dawanqi oil-gas field, Tarim Basin, China. *J. Geoph. Res. Atmos.* **122**, 4353–4363 (2017).
110. Golombek, M.P., Phillips, R.J., Mars tectonics. In: *Planetary Tectonics*, (Thomas R. Watters and Richard A. Schultz, eds.) Cambridge University Press, pp 183–232 (2009).
111. Watters, T.R., Lithospheric flexure and the origin of the dichotomy boundary on Mars. *Geology* **31**, 271–274 (2003).
112. Watters, R.R., Thrust faults along the dichotomy boundary in the eastern hemisphere of Mars. *J Geophys. Res* **108**, doi:10.1029/2002JE001934 (2003).

113. Guest, A., Smrekar, S.E., Relaxation of the martian dichotomy boundary: faulting in the Ismenius Region and constraints on the early evolution of Mars. *J Geophys Res* **110**, E12S25 (2005). doi:10.1029/2005JE002504.
114. McBride, H.H., Leetaru, H.E., Bauer, R.A., Tingey, B.E., Schmidt, S.E.A., Deep faulting and structural reactivation beneath the southern Illinois basin. *Precambrian Res.* **157** (1-4), 289–313 (2007).
115. Grotzinger J. P. et al., Deposition, exhumation, and paleoclimate of an ancient lake deposit, Gale crater, Mars. *Science* **350**, aac7575 (2015). doi: 10.1126/science.aac7575.
116. Siebach, K.L. & Grotzinger, J.P., Volumetric estimates of ancient water on Mount Sharp based on boxwork deposits, Gale crater, Mars. *J. Geophys. Res.* **119**, 189-198 (2014).
117. Andrews-Hanna, J.C., Soto, A. & Richardson, M.I., Meridiani Planum and Gale crater: Hydrology and climate of Mars at the Noachian-Hesperian boundary. *43rd Lunar and Planetary Science Conference*. Abs. # 2706 (2012).
118. Andrews-Hanna, J.C., Soto, A. & Richardson, M.I., The hydrologic and climatic context of the Gale crater sedimentary mound. In: *Proc. 3rd Conference on Early Mars*. Abs. # 7038 (2012).
119. Irwin, R.P. III, Watters, T.R., Howard, A.D., Maxwell, T.A. & Zimbelman, J.R., Origin of Aeolis Mensae, Mars, fretted terrain in a thick sedimentary deposit. *6th Intl. Conf. On Mars*, Abs. # 3092 (2003).
120. Dickson, J.L., Head, J.W. & Marchant, D.R., Late Amazonian glaciation at the dichotomy boundary on Mars: Evidence for glacial thickness maxima and multiple glacial phases. *Geology* **36**, 411–414 (2008).
121. Davila, A.F., et al., Evidence for Hesperian glaciation along the martian dichotomy boundary. *Geology* **41**, 755–758 (2013).
122. Burr, D.M., McEwen, A.S. & Sakimoto, W.E.H., Recent aqueous floods from the Cerberus Fossae, Mars. *Geophys. Res. Lett.* **29** (1), 1013 (2002). doi: 0.1029/2001GL013345.
123. Fonseca, R. M., Zorzano-Mier, M.-P. & Martín-Torres, J., Planetary Boundary Layer and Circulation Dynamics at Gale Crater, Mars. *Icarus* **302**, 537-559 (2018).